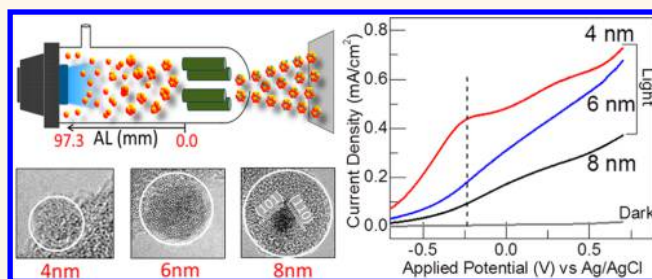


Size-Selected TiO₂ Nanocluster Catalysts for Efficient Photoelectrochemical Water Splitting

Saurabh Srivastava,[†] Joseph Palathinkal Thomas,[†] Md. Anisur Rahman,[†] Marwa Abd-Ellah,[†] Mamata Mohapatra,[‡] Debabrata Pradhan,[§] Nina F. Heinig,[†] and Kam Tong Leung^{*,†}

[†]WATLab and Department of Chemistry, University of Waterloo, Waterloo, Ontario N2L3G1, Canada, [‡]Institute of Minerals & Materials Technology, Bhubaneswar, OD 751013, India, and [§]Materials Science Centre, Indian Institute of Technology, Kharagpur, WB 721302, India

ABSTRACT Nanoclusters (NCs) are of great interest because they provide the link between the distinct behavior of atoms and nanoparticles and that of bulk materials. Here, we report precisely controlled deposition of size-selected TiO₂ NCs produced by gas-phase aggregation in a special magnetron sputtering system. Carefully optimized aggregation length and Ar gas flow are used to control the size distribution, while a quadrupole mass filter provides precise *in situ* size selection (from 2 to 15 nm). Transmission electron microscopy studies reveal that NCs larger than a critical size (~8 nm) have a crystalline core with an amorphous shell, while those smaller than the critical size are all amorphous. The TiO₂ NCs so produced exhibit remarkable photoelectrochemical water splitting performance in spite of a small amount of material loading. NCs of three different sizes (4, 6, and 8 nm) deposited on H-terminated Si(100) substrates are tested for the photoelectrochemical catalytic performance, and significant enhancement in photocurrent density (0.8 mA/cm²) with decreasing NC size is observed with a low saturation voltage of -0.22 V vs Ag/AgCl (0.78 V vs RHE). The enhanced photoconductivity could be attributed to the increase in the specific surface area and increase in the number of active (defect) sites in the amorphous NCs. The unique advantages of the present technique will be further exploited to develop applications based on tunable, size-selected NCs.



KEYWORDS: TiO₂ nanoclusters · size selection · magnetron sputtering · photoelectrochemical catalysts · water splitting reaction

Transition metal and metal oxide nanoclusters (NCs) have attracted a lot of recent attention due to their numerous applications in catalysis, sensors, and optoelectronic and magnetic devices.^{1–8} In the early 1980s, the development of precise mass (or size)-selected nanocluster molecular beam systems has enabled cluster formation with a well-defined size distribution, which has opened up new opportunities for understanding gas-phase reaction dynamics and catalysts.^{9–11} More recently, there has been renewed interest in the deposition of transition metal NCs and the assembly of three-dimensional arrays of discrete size-selected NCs or nanoparticles onto surfaces.^{12–18} These NC assemblies (*i.e.*, nanosystems) allow the chemical properties of these materials to be tuned by controlling their nanoscale cluster/particle size and structure, with further optimization made possible by modifying the

nature of nanoconstituents often combinatorially. Since molecular beam technique has enabled the study of free, unsupported NCs in the gas phase,^{19,20} various procedures have been developed to deposit transition metal NCs onto substrates (or supports) by gas-phase aggregation technique.^{14,16–18} The objective of this deposition approach is to preserve the size of the as-formed NCs on the surfaces. However, acquiring nearly monosized NCs at a few nanometer scale remains a difficult task. Size-tuning of supported transition metal NCs can be used to enhance the catalytic activity at the NC surface and interfacial regions.²¹ A major challenge in the synthesis of stable and well-controlled arrays of size-specific NCs is the inhibition of aggregation on the surface. Early studies have largely focused on metal NCs, including Ag,^{12,14} Au,¹³ Cu,¹⁷ Pd,¹⁸ and Zn²² NCs. In contrast, there are considerably fewer

* Address correspondence to tong@uwaterloo.ca.

Received for review October 7, 2014 and accepted November 3, 2014.

Published online November 03, 2014
10.1021/nn505705a

© 2014 American Chemical Society

studies on metal oxide NCs, particularly titanium dioxide (TiO₂) NCs, and on their size tuning with a narrow size distribution produced by using the general technique of gas-phase aggregation.^{23–26} Lambert's group deposited doped TiO₂ NCs using a gas-condensation technique in an oxygen and methane ambient conditions.¹⁶ Using a gas-aggregation source, Drabik *et al.* produced Ti NCs in lower vacuum conditions, which then became oxidized in ambient conditions.²⁴

High chemical stability and low-cost production have made TiO₂ one of the most widely used photocatalytic materials since the first report of water splitting using TiO₂ by Fujishima and Honda over 30 years ago.²⁷ TiO₂ is also one of the most studied transparent conductive oxides, with band gaps of 3.02 eV for rutile and 3.2 eV for anatase structures.²⁸ With the bottom of the conduction band more negative than the redox potential of H₂/H₂O (0 V) and the top of the valence band more positive than the redox potential of H₂O/O₂ (–1.23 V),^{27–30} TiO₂ is possibly the “ideal” photocatalyst for the photoelectrochemical water splitting reaction. Different types of TiO₂ nanostructures, including nanoparticles and nanowires, and thin films have been tested for the water splitting reaction but were found to produce a photocurrent density no greater than 0.1 mA/cm².^{30–32} An assembly of discrete NCs would be of great interest because of its high specific surface area that provides a large number of reaction sites (per volume) for electron–hole pair generation for water splitting reaction upon light illumination.

As Ti and its oxides are of great importance to catalysis and nanoelectronics, the synthesis of stable, size-selected Ti and TiO₂ NCs in a controlled way could offer new prospects for creating novel cluster-assembled materials with desirable properties for electronic and optoelectronic applications, including memory devices, fuel cells, and solar cells. Here, we present a new fabrication process to produce well-ordered, precisely size-selected, monosized NCs with excellent uniformity over a large area using a novel NC magnetron sputter source with a quadrupole mass filter built in. We further demonstrate the exceptional photoelectrochemical catalytic performance of these high-quality TiO₂ NCs as photoanodes in a water splitting reaction.

RESULTS AND DISCUSSION

In our experiment, size-selected NCs with specified mass-to-charge ratios are successfully synthesized by using the Nanogen source, shown schematically in Figure 1. Figure 2a shows the average NC size (diameter) as a function of the Ar gas flow for different aggregation lengths (ALs). In spite of the small exit aperture (3 mm diameter) of the Nanogen source, the pressure at which the NCs are deposited on the substrate (in the deposition chamber) depends linearly on the Ar gas flow during growth (Figure 2a). The Ar gas

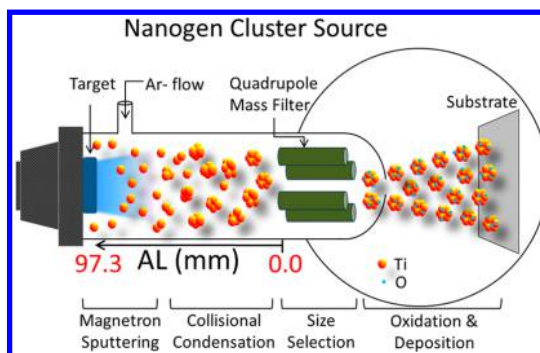


Figure 1. Schematic diagram of the production of a size-selected cluster beam in the Nanogen cluster source (not drawn to scale), which involves the following steps: (a) generation of Ti_n moieties and their ions by magnetron sputtering, (b) collisional condensation that leads to nucleation and gas aggregation, and eventually to Ti_n and Ti_n⁺ cluster formation, and (c) size selection of Ti_n⁺ cluster ions by a quadrupole mass filter. The Ti_n⁺ cluster ions exiting the aggregation (or Nanogen source) chamber from a 3 mm diameter aperture become oxidized by ambient conditions in the deposition chamber, and the resulting TiO₂ cluster ions are then deposited and neutralized on the substrate under soft-landing conditions (*i.e.*, without any bias applied to the sample) to produce the size-selected TiO₂ nanoclusters. The aggregation length, defined as the separation between the front face of the target and the entrance plane of the quadrupole, and the Ar gas flow are the main parameters used to control the overall cluster size distribution before size selection. No bias is applied to the substrate to ensure soft landing of the nanoclusters.

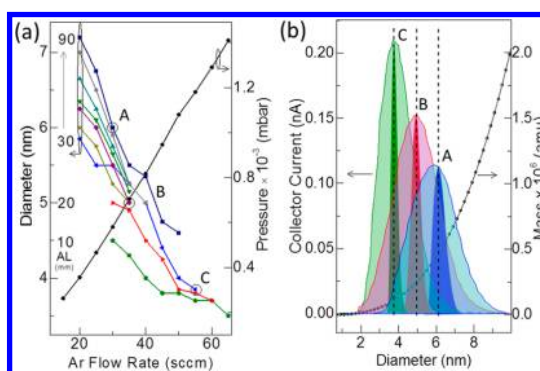


Figure 2. (a) Cluster size (left axis) and deposition chamber pressure (right axis) as a function of Ar flow rate for different aggregation length from 10 to 90 mm, in steps of 10 mm, and (b) typical nanocluster size distributions, as represented by quadrupole collector current (left axis), obtained with three typical combinations of (AL, Ar flow rate) as marked by large open circles in (a): A = (80 mm, 30 sccm), B = (60 mm, 35 sccm), and C = (20 mm, 55 sccm). The vertical dashed line marks the respective mode cluster size of each nanocluster distribution, while the corresponding sharpened peak marked by the darkened area corresponds to the distribution of nanoclusters, mass-selected (within 2% of the mode cluster size) by applying an appropriate set of dc and ac voltages to the quadrupole mass filter. The total mass (right axis) as a function of nanocluster size produced by the Nanogen cluster source is also shown.

pressure is found to have the largest effect on the growth kinetics of the NCs. The system can therefore be optimized to provide the desired cluster size by controlling the Ar flow rate in the aggregation chamber. Not only does the Ar gas flow help to initiate the

plasma for sputtering to occur, but Ar also works as a carrier gas to support the growth of the NCs by providing them nucleation centers in the gas phase and to carry them toward the substrate. The aggregation chamber provides the important space needed for the target source atoms to undergo collisional condensation.³³ This space can be physically adjusted by changing the AL, which corresponds to the target-to-quadrupole separation (Figure 1). As a general rule, an increase in the Ar flow causes a decrease in the NC size because the clusters are swept out of the aggregation chamber faster before the clusters have sufficient time to self-condense to a larger size. Figure 2a shows an almost linear decrease in cluster size with increasing Ar flow rate for all ALs from 10 to 90 mm. We observe that AL also affects the size distribution of resulting NCs. For a fixed Ar flow rate, the cluster size increases with increasing AL (Figure 2a). This is consistent with our expectation that a bigger aggregation volume provided by a larger AL allows the Ti atoms in transit to reside in the aggregation chamber longer, thereby facilitating more collisional encounters to form larger clusters. Our present study, therefore, shows that the smallest cluster size can be achieved by maintaining a high Ar flow for a short AL. Conversely, the larger cluster size can be obtained by employing a lower carrier gas flow for a longer AL. As illustrated in Figure 2a, the cluster size can be tuned in the range below 10 nm and a cluster size as small as 3 nm can be easily obtained. This size regime is smaller than the TiO₂ NCs reported earlier.^{14,16–18,25,34}

Figure 2b shows the relative populations of NCs as formed in the gas phase as a function of NC size for three typical (AL, Ar flow) combinations: A = (80 mm, 30 sccm), B = (60 mm, 35 sccm), and C = (20 mm, 55 sccm). The relative population of the NCs is indicated by the quadrupole collector current. A near-Gaussian size distribution is clearly observed for all (AL, Ar flow) sets. As the mode cluster size (marked by the peak maximum) increases, the peak collector current decreases with concomitant increase in the width of its distribution, from set C to set B to set A. Upon applying an appropriate set of voltages to the quadrupole mass filter, the cluster size distribution can be dramatically narrowed to a sharp profile as defined by the mass resolution of the quadrupole, which demonstrates the effectiveness of mass selection by the quadrupole mass filter. Figure 2b also shows that the cluster mass increases quadratically with increasing cluster size.

Figure 3a–c shows tapping-mode AFM images of TiO₂ NCs deposited on H–Si substrates along with their size distributions at mode cluster sizes of 3.5, 5.0, and 6.2 nm, respectively, obtained with appropriate (AL, Ar flow rate) settings. With the spatial resolution of AFM generally larger than 10 nm, we estimate the size (diameter) of the as-deposited NCs from their

respective height profiles, assuming a spherical shape for these NCs. A near-Gaussian size distribution (obtained without the use of the quadrupole mass filter) is clearly observed for all three mode sizes. The size distributions obtained from our AFM measurements for the as-deposited NCs are also found to be in good accord with and therefore validate those as reflected by the collector current profiles of the quadrupole mass filter (Figure 2b).

The impact energy of the NCs is one of the key parameters in cluster–surface collisions. Given the kinematics of the system, the TiO₂ NCs should undergo soft landing onto the substrate because the NCs impinging onto the substrate are very small in size and their kinetic energy at room temperature is less than 0.1 eV.^{20,35} The deposited NCs should therefore have their stoichiometry preserved, without any change to their chemical or physical properties, and they are not expected to undergo further diffusion into the bulk upon physisorption. In the present work, no bias is applied on the substrate to maintain low impinging energy of the NCs to the substrate, thereby ensuring a soft landing condition. Furthermore, it should be possible to produce TiO₂ NCs of the same cluster size but with different aerial density by simply manipulating different (AL, Ar flow) combinations for the same deposition time. To demonstrate this unique control provided by the present technique of NC generation, we show, in Figure 3d–f, three different densities obtained for NCs with essentially the same mode cluster size of 5 nm. The variation in the densities of these NCs with the same mode size can be understood in terms of the kinematics of the NCs produced under different conditions. In particular, the kinetic energy of the impinging NCs could significantly affect the nature/type of the event that follows. For a high Ar flow rate and a larger AL, less energetic NCs will be produced. This is because of the resulting larger number of collisions among clusters themselves and/or with the wall of the aggregation chamber over a longer period of time. This low kinetic energy regime ensures soft landing without any subsequent diffusion on the surface and/or into the bulk. On the other hand, in the other limit of a low Ar flow rate and a smaller AL, more energetic NCs will be generated because of less resulting collisional encounters. Some of the NCs could also bounce backward due to head-on collisions with the surface, thereby reducing the cluster density on the surface. The areal density can also be controlled by the amount of deposition time, while keeping other preparation conditions the same to ensure that the clusters physisorb under soft-landing conditions and without any cluster aggregation (Supporting Information, Figure S1) and also without any deformation from spherical shape (as observed by TEM, Figure 5d) on the surface. The present technique of NC generation therefore provides a sensitive control of the relative kinetic

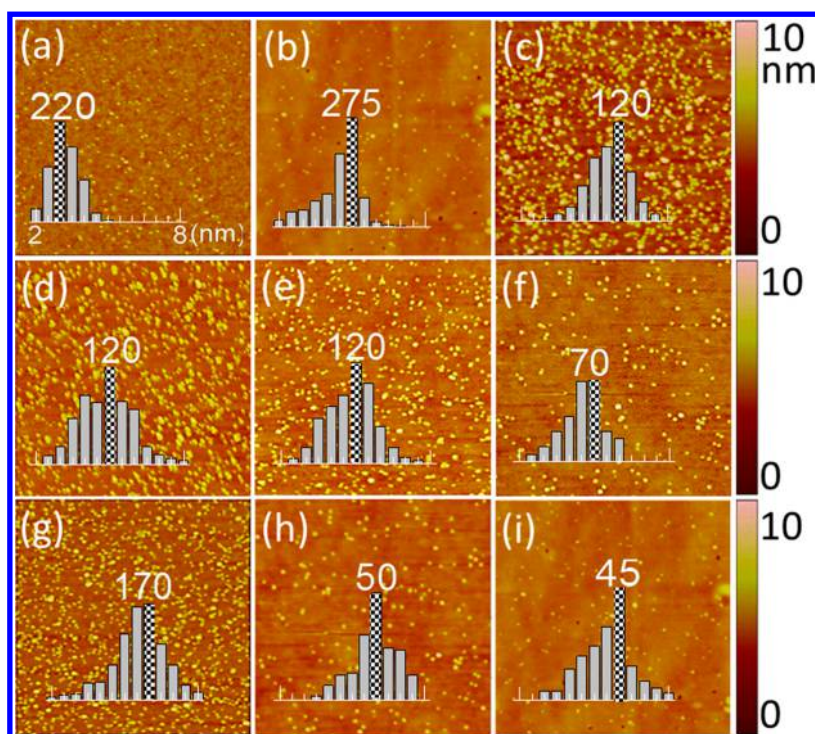


Figure 3. AFM images of size-selected TiO_2 nanoclusters obtained with mode sizes of (a) 3.5 nm, (b) 5 nm, and (c) 6.2 nm (deposited with appropriate growth conditions) and with a mode size of 5 nm deposited with three different growth conditions (AL, Ar flow): (d) (80 mm, 40 sccm), (e) (60 mm, 35 sccm), and (f) (20 mm, 30 sccm), all on H–Si substrates. AFM images of size-selected TiO_2 nanoclusters with a mode size of 6 nm deposited on three different substrates: (g) H–Si, (h) glass, and (i) quartz. All AFM images are obtained for a scanned area of $1 \times 1 \mu\text{m}^2$. Insets show the corresponding histograms for the cluster size distributions of the nanoclusters from 2 to 8 nm obtained under appropriate (AL, Ar flow) combinations, with the peak marked by the numbers of the clusters with the respective mode sizes.

energy of NCs in the gas phase in the soft-landing regime.

The adhesion properties of TiO_2 toward different types of substrate surfaces are further investigated by depositing TiO_2 NCs on three different substrates simultaneously under the same deposition conditions. Figure 3g–i compares the areal densities of TiO_2 NCs deposited on H–Si, glass, and quartz substrates. The sizes of NCs on all three substrates are found to be similar (6 nm), consistent with the mode size as selected by the appropriate (AL, Ar flow) combination of (80 mm, 30 sccm). Interestingly, the areal density of the NCs on H–Si ($\sim 750/\mu\text{m}^2$) is considerably higher than those on glass ($\sim 180/\mu\text{m}^2$) and quartz substrates ($\sim 170/\mu\text{m}^2$). This is consistent with the higher sticking coefficient of TiO_2 thin film on H–Si when compared to those on the other two oxide surfaces. The NC densities for glass and quartz are similar because of the similar chemical nature of these oxide surfaces. Despite the expected high propensity of TiO_2 on the oxide surface to aggregate due to its higher enthalpy compared to that of the oxide surfaces,¹⁹ we see no evidence of cluster aggregation on the surface even after deposition for a longer time (Figure S1), with individual NCs remaining uniformly distributed over the entire surface. This further confirms the soft-landing condition provided by the Nanogen cluster source. The

deposition time can therefore be used to control the surface coverage, that is, the aerial density of the NCs (which is important to their application as catalysts), and therefore the resulting surface roughness. The root mean square (rms) surface roughness is estimated from AFM measurement for samples obtained with different deposition times (Supporting Information, Table S1) and found to increase with increasing deposition time from 15 to 20 to 30 min, followed by a decrease after 60 min of deposition. The latter reduction in rms roughness could be due to increase in the packing efficiency.

To characterize the chemical nature of the nanoclusters, we show, in Figure 4a, the XPS spectra of the Ti 2p region collected as a function of sputtering time for a typical TiO_2 NC film deposited with a mode size of 6 nm on H–Si for 60 min. The prominent Ti 2p_{3/2} peak at 459.2 eV corresponds to the Ti^{4+} state attributable to TiO_2 , in good accord with an earlier report.³⁶ The minor shift in the spectrum to a higher binding energy after a brief 5 s of sputtering is due to the removal of surface hydrocarbons commonly present as a result of ambient handling. Upon sputtering for a total of 20 s, a weak Ti 2p_{3/2} feature emerges at 457.5 eV and becomes more intense, while the Ti^{4+} feature is weakened upon sputtering for 90 s. This intermediate feature at 457.5 eV, tentatively assigned to Ti^{3+} , becomes reduced

in intensity and appears to shift toward a lower binding energy (454.3 eV) upon further sputtering for 270 s. Continued sputtering for 450 and 650 s causes emergence of a well-defined Ti $2p_{3/2}$ feature at 454.3 eV, which could be assigned to TiO. The Ti $2p_{3/2}$ features located at the intermediate peak position (between Ti^{4+} and Ti^{2+} states) could therefore be attributed to TiO_x ($2 > x < 1$), which corresponds to nonstoichiometric Ti oxide phases due to the reduction of Ti^{4+} to Ti^{3+} and Ti^{2+} by Ar-ion bombardment.³⁶ This ion-induced reduction is also confirmed, in our separate experiment, by depth-profiling XPS analysis of commercial

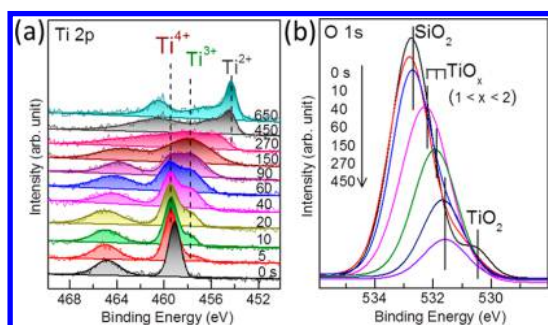


Figure 4. XPS spectra of (a) Ti 2p and (b) O 1s regions for TiO_2 nanoclusters as-deposited on a H-Si substrate and as a function of Ar sputtering time. Only the Ti $2p_{3/2}$ region is used in (a) to identify various chemical states of the nanoclusters.

TiO_2 powders (Aldrich, 99.99% purity) (Supporting Information, Figure S2a). Figure 4b shows the corresponding XPS spectra of the O 1s region as a function of sputtering time for the NC sample. Before sputtering, the O 1s spectrum exhibits two peaks at 530.6 and 532.8 eV, which are consistent with the assignment to TiO_2 and SiO_2 (the latter corresponding to native oxide on the Si substrate), respectively. After 40 s of sputtering, the O 1s feature for native SiO_2 (at 532.8 eV) is evidently removed. The O 1s feature for TiO_2 appears to shift to a higher binding energy with increasing sputtering time, in a similar manner as the Ti $2p_{3/2}$ feature in Figure 4a, which confirms the emergence of suboxide (TiO_x) phases due to reduction of TiO_2 . The corresponding Si 2p spectrum is found to be dominated by a major Si peak at 99.3 eV and a minor SiO_x peak at 103.2 eV due to native oxide (Supporting Information, Figure S2b).

To demonstrate the photoelectrochemical catalytic properties, we employ the TiO_2 NCs deposited with different mode sizes on H-Si as the photoanode in a water splitting reaction. All the photocurrent measurements are conducted for an illumination area of $5 \times 5 \text{ mm}^2$ with a power density of 50 mW/cm^2 . The photoelectrochemical water splitting mechanism is described schematically in Figure 5a. In a water splitting reaction, photoexcitation occurs at the TiO_2 NC photoanode, which is immersed in an aqueous electrolyte along with the Pt counter electrode (and a

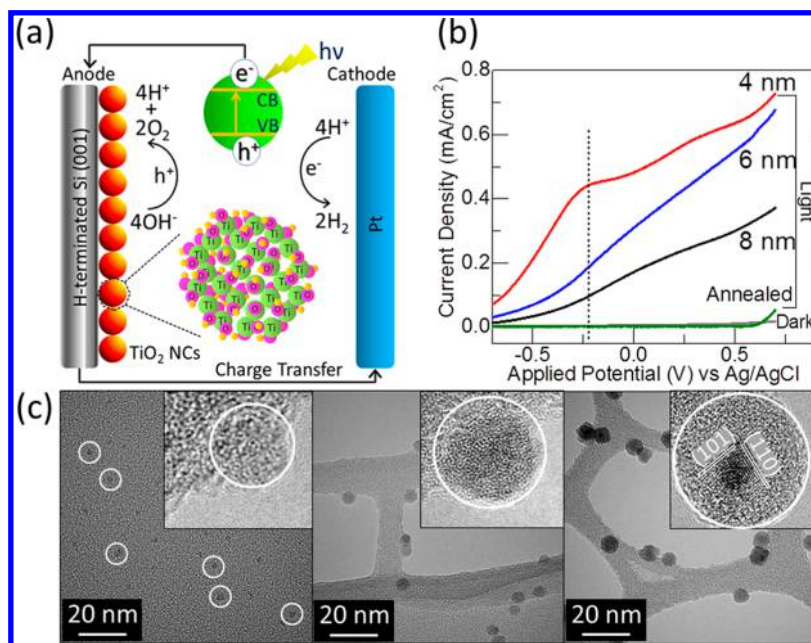


Figure 5. (a) Schematic diagram of the mechanism of a photoelectrochemical water splitting reaction. An expanded view of a TiO_2 nanocluster (NC, red sphere), consisting of Ti (green spheres), O (pink spheres), and H atoms (brown spheres), is shown as the bottom inset. The top inset shows the electron-hole pair generation in TiO_2 upon UV-vis light illumination, which supplies holes (h^+) for the oxidation of OH^- leading to O_2 evolution at the photoanode and electrons (e^-), upon traveling to the counter electrode through an external circuit, for reduction leading to H_2 generation. (b) Photocurrent densities as a function of applied potential obtained in a photoelectrochemical water splitting reaction in a 5 M KOH electrolyte, using TiO_2 nanoclusters of different sizes (4, 6, and 8 nm) and the post-annealed TiO_2 nanoclusters (6 nm), all on H-Si, as the photoanodes, all with an illumination area of $5 \times 5 \text{ mm}^2$ under a 300 W Xe lamp at a power density of 50 mW/cm^2 . (c) TEM images of 4 nm (left), 6 nm (center), and 8 nm nanoclusters (right) deposited directly on holey carbon TEM grids, along with high-resolution images shown as insets illustrating their respective degrees of crystallinity.

Ag/AgCl reference electrode). Electrons and holes are generated when the TiO₂ NC is illuminated with UV–vis light, which facilitates redox reactions (oxidation at the photoanode and reduction at the counter electrode) at the NC–water interface in the electrolyte and leads to hydrogen (H₂) evolution. Figure 5b shows the photocurrent density as a function of applied potential for the TiO₂ NC/H–Si working electrode in 5 M KOH in the dark and under illumination of a xenon lamp. Nanoclusters with three different NC sizes (4, 6, and 8 nm), preselected by using the quadrupole mass filter, are chosen to illustrate the cluster size effect on the photoelectrochemical performance. Evidently, a significant enhancement in the photocurrent density with decreasing NC size is observed. We attribute this to the interplay between the effect of the increase in the specific surface area and that of the increase in the amount of active sites due to the increased amorphicity of the NCs with decreasing size. The TEM images shown in Figure 5c illustrate the remarkable homogeneity of the NCs, all with nearly identical size, which further verifies the precise size selection achieved by using the quadrupole mass filter. Furthermore, the larger NC (8 nm) is found to consist of a crystalline core surrounded by an amorphous shell, while the smaller NCs (6 and 4 nm) below a critical size appear to be completely amorphous. The amorphous nature of the smaller NCs gives rise to a higher density of defects, which work as trapping and recombination centers for the photogenerated electron–hole pairs. To confirm that amorphous TiO₂ NCs are better suited for water splitting reaction, we prepare, in a separate experiment, a “post-annealed” TiO₂ NC sample by annealing the as-deposited 6 nm NCs at 800 °C for 90 min in air. A substantial drop in the photocurrent density is observed for the post-annealed sample (Figure 5b). This is due to the reduction in the defect density as a result of improved crystallinity caused by annealing at a high temperature. The increase in the photocurrent density of the totally amorphous 6 nm NCs with respect to that of the crystalline core/amorphous shell 8 nm NCs is attributed to both of the aforementioned effects, while the further enhancement found for the 4 nm NCs with respect to the 6 nm NCs, both of which are totally amorphous, is due to the effect arising from an increase in the specific surface area. Since the surface area plays an important role in photoelectrochemical catalysis, substrate coverages (*i.e.*, the amount of NC loading on the substrate) by TiO₂ nanoclusters for all three samples deposited for 15 min on H–Si substrates are calculated by using the ImageJ software. Approximately 20% coverage is observed for all three samples, which suggests that there is a lot of room for potential improvement in the photoelectrochemical performance.

The saturation voltage for the 4 nm NCs is observed to be -0.22 V vs Ag/AgCl (or 0.78 V vs RHE), which is

well within the range of the typical values of 0.5 – 0.8 V vs RHE found for other TiO₂ nanomaterials.^{30,37–39} We obtain a photoconversion efficiency (PCE) of $\sim 0.43\%$ (Supporting Information, Figure S3a) and a total PCE, as-estimated according to earlier reports,^{29,40} of $\sim 1.0\%$, at an applied potential of 0.78 V vs RHE. For TiO₂ nanotubes and other nanostructures, their corresponding total PCEs are in the range of 0.2 – 3.0% . For TiO₂ NCs, the present PCE of 1.0% is the highest ever observed for this type of nanoclusters, and it is comparable to most of these nanomaterials reported in the literature.^{38,41–48} This performance is especially remarkable when considering the very tiny amount of TiO₂ NCs on the substrate, all of which are prepared without any post-synthesis modification or treatment (as often required in earlier work). It should be noted that most of the samples reported in the literature^{38,44–48} are based on TiO₂ or other metal oxide nanowires or nanotubes with post-modification and these samples contain a significant (large) amount of materials, which provide a large number of active sites for the photoelectrochemical reaction. In our case, the PCE could potentially be enhanced at least 5 times by increasing the amount of cluster loading from 20% coverage to a monolayer coverage (*e.g.*, by increasing the amount of deposition time). Indeed, a theoretical PCE of 5% would put our NC samples (with just one monolayer of coverage) to be among the top photoelectrochemical catalysis performers based on TiO₂ nanomaterials for the water splitting reaction. Even higher PCE can be obtained with multiple layers of TiO₂ NCs (as was commonly employed for other TiO₂ nanomaterials in earlier reports). Furthermore, we can also potentially increase the PCE further by employing nanoclusters with even smaller size and by modifying the clusters with chemical functionalization. Fabricating hybrid and/or core–shell NCs and synthesizing binary or tertiary NC systems could also enhance the PCE and can be easily realized using the present Nanogen cluster source (equipped with the triple target capability).

CONCLUSIONS

We have successfully fabricated and deposited size-selected TiO₂ NCs on three different substrates (H–Si, glass, and quartz) at room temperature under soft-landing conditions using a magnetron-based nanocluster source equipped with a quadrupole mass filter. The growth process of the NCs is studied by depositing the nanoclusters under different growth conditions and by studying their growth environment. On all the substrates employed in the present work, the TiO₂ NCs are found to be essentially monosized and uniformly distributed over the entire surface (without agglomeration), and no surface diffusion of the NCs is observed. The use of a high vacuum system and the precise control over aggregation length and Ar flow have enabled us to produce TiO₂ NCs with an

unprecedented high degree of purity (as verified by XPS) and excellent uniformity in size and distribution (as demonstrated by AFM and TEM). Size-tuning experiments on H–Si substrates indicate that we also have excellent control and reproducibility for the desired NC size. A higher photoelectrochemical catalytic activity for the water splitting reaction is obtained when the NC size is below 6 nm and its activity is higher than the large size TiO₂ NCs. As the

NC size is reduced, the increase in specific surface area and the greater amorphicity of the NCs both contribute to the enhanced photoelectrochemical performance. The Nanogen magnetron cluster source coupled with a quadrupole mass filter is therefore a promising versatile tool for producing high-purity, size-selected, ultrasmall TiO₂ NCs (below 10 nm) for application in catalysis, nanoelectronics, and nanobiosensors.

MATERIALS AND METHODS

Size-selected TiO₂ NCs are produced using a gas-condensation technique with a gas-aggregation cluster source based on dc magnetron sputtering (Nanogen 50, Mantis Deposition Ltd.),³³ which employs the Haberland concept of cluster formation.^{19,20} A schematic diagram of the Nanogen source is shown in Figure 1. A titanium target (99.95% purity, ACI Alloys) is mounted in the cluster source chamber with a base pressure of 1×10^{-8} mbar. A broad beam of Ti atoms is generated by dc magnetron sputtering (at 55 mA) in Ar, and these sputtered atoms condense into clusters under high collision-prone ambient conditions. The cluster growth involves two basic steps: (a) generation of Ti atoms, particle fragments, and ions by magnetron sputtering, which then undergo (b) collisional condensation, involving nucleation and gas-phase aggregation leading to cluster formation.²⁰ Cluster growth can be controlled by varying the Ar gas pressure and the aggregation length in the condensation zone of the aggregation chamber (where cluster formation occurs as a result of collisions of atoms with one another). Since a large fraction of the NCs generated by the Nanogen source is negatively charged, it is possible to provide precise mass selection of NCs of a particular size based on their mass-to-charge ratios by using a quadrupole mass filter in the NC source. A set of ac and dc voltages is applied to the quadrupole filter, with 2% mass resolution and throughput up to 10^6 amu, to facilitate an oscillating path that allows passage of cluster ions of the selected size. After exiting the aggregation chamber through an orifice (3 mm diameter), the cluster ions are neutralized and collected on the substrate positioned 70 mm in front of the orifice in the deposition chamber. The input flow rate of the Ar gas in the Nanogen source is used to control the (deposition) chamber pressure (10^{-4} to 10^{-3} mbar) at which the deposition process occurs. In particular, the input Ar flow rate directly affects the processes in the condensation zone and the efficiency of the clusters emerging from the aggregation chamber.¹⁸ Cluster sizes of 2–15 nm (diameter) can be produced using the Nanogen source. Here, we focus on monosized clusters smaller than 8 nm and investigate the size dependency of these ultrasmall NCs in the present work. The substrates used for the present work are H-terminated Si(100) (denoted as H–Si), quartz, and float glass. All the substrates are cleaned ultrasonically in acetone and isopropyl alcohol before use, while the Si substrate is also rinsed in 2% HF for 10 min to remove the native oxide layer and to produce H-termination on the Si substrate (H–Si).

The surface morphology and the size of the NCs are characterized *ex situ* by atomic force microscopy (AFM) operated in tapping mode in a Digital Instruments Dimension 3100 Nanoman Nanoscope IV microscope, while the crystallinity of the NCs is determined by transmission electron microscopy (TEM) in a JEOL 2010F microscope operated at 200 kV. TEM samples are prepared by directly depositing the NCs onto a holey carbon TEM grid. Chemical-state composition is analyzed by X-ray photoelectron spectroscopy (XPS) as a function of Ar-ion sputtering time in a Thermo-VG Scientific ESCALab 250 microprobe, equipped with a monochromatic Al K α X-ray source (1486.6 eV). Ar-ion sputtering is performed over a raster area of 3×3 mm² at an ion beam energy of 3 keV and a typical sample current density of 110 nA/mm². The XPS data are fitted by using Casa

XPS software with a Shirley background. The photoelectrochemical water splitting experiments are performed by using a CH Instruments 660A electrochemical station in a three-electrode quartz cell with an electrolyte solution of 5 M KOH (prepared from analytical grade KOH and Millipore water at room temperature). Photocurrents are measured with the size-selected NCs deposited on a substrate as the working electrode (*i.e.*, the photoanode), both in the dark and under the illumination of a 300 W xenon lamp (300–1000 nm, Oriel Instruments 6258) with an AM 1.5 filter. A minimum power density of 50 mA/cm² is delivered to the sample. Ag/AgCl (3 M KCl) and Pt are used as the reference and counter electrodes, respectively.

Conflict of Interest: The authors declare no competing financial interest.

Acknowledgment. This work was supported by the Natural Sciences and Engineering Research Council (NSERC) of Canada.

Supporting Information Available: Additional AFM images of TiO₂ nanoclusters deposited on H–Si; roughness estimation; XPS spectra of TiO₂ powder (anatase); and photoelectrochemical catalytic performance data. This material is available free of charge *via* the Internet at <http://pubs.acs.org>.

REFERENCES AND NOTES

- Schmid, G.; Bäuml, M.; Geerkens, M.; Heim, I.; Osemann, C.; Sawitowski, T. Current and Future Applications of Nanoclusters. *Chem. Soc. Rev.* **1999**, *28*, 179–185.
- Schmid, G. Nanoclusters—Building Blocks for Future Nanoelectronic Devices?. *Adv. Eng. Mater.* **2001**, *3*, 737–743.
- Ott, L. S.; Finke, R. G. Transition-Metal Nanocluster Stabilization for Catalysis: A Critical Review of Ranking Methods and Putative Stabilizers. *Coord. Chem. Rev.* **2007**, *251*, 1075–1100.
- Enterkin, J. A.; Poeppelmeier, K. R.; Marks, L. D. Oriented Catalytic Platinum Nanoparticles on High Surface Area Strontium Titanate Nanocuboids. *Nano Lett.* **2011**, *11*, 993–997.
- Habibpour, V.; Wang, Z. W.; Palmer, R. E.; Heiz, U. Size-Selected Metal Clusters: New Models for Catalysis with Atomic Precision. *J. Appl. Sci.* **2011**, *11*, 1164–1170.
- Li, J.; Guo, S.; Wang, E. Recent Advances in New Luminescent Nanomaterials for Electrochemiluminescence Sensors. *RSC Adv.* **2012**, *2*, 3579–3586.
- Aluri, G. S.; Motayed, A.; Davydov, A. V.; Oleshko, V. P.; Bertness, K. A.; Sanford, N. A.; Mulpuri, R. V. Methanol, Ethanol and Hydrogen Sensing Using Metal Oxide and Metal (TiO₂–Pt) Composite Nanoclusters on GaN Nanowires: A New Route towards Tailoring the Selectivity of Nanowire/Nanocluster Chemical Sensors. *Nanotechnology* **2012**, *23*, 175501–175512.
- Heiliger, C.; Czerner, M.; Klar, P. J.; Hara, S. Magnetic Sensor Devices Based on Ordered Planar Arrangements of MnAs Nanocluster. *IEEE Trans. Magn.* **2010**, *46*, 1702–1704.
- Sattler, K.; Muhlbach, J.; Recknagel, E. Generation of Metal Clusters Containing from 2 to 500 Atoms. *Phys. Rev. Lett.* **1980**, *45*, 821–824.

10. Dietz, T. G.; Duncan, M. A.; Powers, D. E.; Smalley, R. E. Laser Production of Supersonic Metal Cluster Beams. *J. Chem. Phys.* **1981**, *74*, 6511–6512.
11. Heer, W. A. The Physics of Simple Metal Clusters: Experimental Aspects and Simple Models. *Rev. Mod. Phys.* **1993**, *65*, 611–676.
12. Bromann, K.; Felix, C.; Brune, H.; Harbich, W.; Monet, R.; Buttet, J.; Kern, K. Controlled Deposition of Size-Selected Silver Nanoclusters. *Science* **1996**, *274*, 956–958.
13. Valden, M.; Lai, X.; Goodman, D. W. Onset of Catalytic Activity of Gold Clusters on Titania with the Appearance of Nonmetallic Properties. *Science* **1998**, *281*, 1647–1650.
14. Palmer, R. E.; Pratontep, S.; Boyen, H. G. Nanostructured Surfaces from Size-Selected Clusters. *Nat. Mater.* **2003**, *2*, 443–448.
15. Claridge, S. A.; Castleman, A. W.; Khanna, S. N.; Murray, C. B.; Sen, A.; Weiss, P. S. Cluster-Assembled Materials. *ACS Nano* **2009**, *3*, 244–255.
16. In, S.; Kean, A. H.; Orlov, A.; Tikhov, M. S.; Lambert, R. M. A Versatile New Method for Synthesis and Deposition of Doped, Visible Light-Activated TiO₂ Thin Films. *Energy Environ. Sci.* **2009**, *2*, 1277–1279.
17. Gracia-Pinilla, M.; Martínez, E.; Vidaurri, G. S.; Pérez-Tijerina, E. Deposition of Size-Selected Cu Nanoparticles by Inert Gas Condensation. *Nanoscale Res. Lett.* **2009**, *5*, 180–188.
18. Ayes, A. I.; Qamhieh, N.; Ghamlouche, H.; Thaker, S.; El-Shaer, M. Fabrication of Size-Selected Pd Nanoclusters Using a Magnetron Plasma Sputtering Source. *J. Appl. Phys.* **2010**, *107*, 034317.
19. Haberland, H.; Karrais, M.; Mall, M. A New Type of Cluster and Cluster Ion Source. *Z. Phys. D: At., Mol. Clusters* **1991**, *20*, 413–415.
20. Haberland, H.; Mall, M.; Moseler, M.; Qiang, Y.; Reiners, T.; Thurner, Y. Filling of Micron-Sized Contact Holes with Copper by Energetic Cluster Impact. *J. Vac. Sci. Technol., A* **1994**, *12*, 2925–2930.
21. Lang, S. M.; Bernhardt, T. M. Gas Phase Metal Cluster Model Systems for Heterogeneous Catalysis. *Phys. Chem. Chem. Phys.* **2012**, *14*, 9255–9269.
22. Thangadurai, P.; Zergioti, I.; Saranu, S.; Chandrinou, C.; Yang, Z.; Tsoukalas, D.; Kean, A.; Boukos, N. ZnO Nanoparticles Produced by Novel Reactive Physical Deposition Process. *Appl. Surf. Sci.* **2011**, *257*, 5366–5369.
23. Shyjumon, I.; Gopinadhan, M.; Helm, C. A.; Smirnov, B. M.; Hippler, R. Deposition of Titanium/Titanium Oxide Clusters Produced by Magnetron Sputtering. *Thin Solid Films* **2006**, *500*, 41–51.
24. Drabik, M.; Choukourov, A.; Artemenko, A.; Polonskyi, O.; Kylian, O.; Kousal, J.; Nichtova, L.; Cimrova, V.; Slavinska, D.; Biederman, H. Structure and Composition of Titanium Nanocluster Films Prepared by a Gas Aggregation Cluster Source. *J. Phys. Chem. C* **2011**, *115*, 20937–20944.
25. Marek, A.; Valter, J.; Kadlec, S.; Vyskočil, J. Gas Aggregation Nanocluster Source—Reactive Sputter Deposition of Copper and Titanium Nanoclusters. *Surf. Coat. Technol.* **2011**, *205*, S573–S576.
26. Drábik, M.; Choukourov, A.; Artemenko, A.; Kousal, J.; Polonskyi, O.; Solař, P.; Kylián, O.; Matoušek, J.; Pešička, J.; Matolinová, I.; Slavinská, D.; Biederman, H. Morphology of Titanium Nanocluster Films Prepared by Gas Aggregation Cluster Source. *Plasma Process. Polym.* **2011**, *8*, 640–650.
27. Fujishima, A.; Honda, K. Electrochemical Photolysis of Water at a Semiconductor Electrode. *Nature* **1972**, *238*, 37–38.
28. Grätzel, M. Photoelectrochemical Cells. *Nature* **2001**, *414*, 338–344.
29. Khan, S. U. M.; Al-Shahry, M.; Ingler, W. B. Efficient Photochemical Water Splitting by a Chemically Modified N-TiO₂. *Science* **2002**, *297*, 2243–2245.
30. Peng, Q.; Kalanyan, B.; Hoertz, P. G.; Miller, A.; Kim, D. H.; Hanson, K.; Alibabaei, L.; Liu, J.; Meyer, T. J.; Parsons, G. N.; Glass, J. T. Solution-Processed, Antimony-Doped Tin Oxide Colloid Films Enable High-Performance TiO₂ Photoanodes for Water Splitting. *Nano Lett.* **2013**, *13*, 1481–1488.
31. Cowan, A. J.; Tang, J.; Leng, W.; Durrant, J. R.; Klug, D. R. Water Splitting by Nanocrystalline TiO₂ in a Complete Photoelectrochemical Cell Exhibits Efficiencies Limited by Charge Recombination. *J. Phys. Chem. C* **2010**, *114*, 4208–4214.
32. Cowan, A. J.; Barnett, C. J.; Pendlebury, S. R.; Barroso, M.; Sivula, K.; Grätzel, M.; Durrant, J. R.; Klug, D. R. Activation Energies for the Rate-Limiting Step in Water Photooxidation by Nanostructured α -Fe₂O₃ and TiO₂. *J. Am. Chem. Soc.* **2011**, *133*, 10134–10140.
33. Nanocluster Deposition Systems, www.mantisdeposition.com.
34. Rai, A. K.; Anh, L. T.; Gim, J.; Mathew, V.; Kang, J.; Paul, B. J.; Song, J.; Kim, J. Simple Synthesis and Particle Size Effects of TiO₂ Nanoparticle Anodes for Rechargeable Lithium Ion Batteries. *Electrochim. Acta* **2013**, *90*, 112–118.
35. Carroll, S.; Hall, S.; Palmer, R. E.; Smith, R. Energetic Impact of Size-Selected Metal Cluster Ions on Graphite. *Phys. Rev. Lett.* **1998**, *81*, 3715–3718.
36. Hashimoto, S.; Tanaka, A. Alteration of Ti 2p XPS Spectrum for Titanium Oxide by Low-Energy Ar Ion Bombardment. *Surf. Interface Anal.* **2002**, *34*, 262–265.
37. Shi, J.; Hara, Y.; Sun, C.; Anderson, M. A.; Wang, X. Three-Dimensional High-Density Hierarchical Nanowire Architecture for High-Performance Photoelectrochemical Electrodes. *Nano Lett.* **2011**, *11*, 3413–3419.
38. Wang, G.; Wang, H.; Ling, Y.; Tang, Y.; Yang, X.; Fitzmorris, R. C.; Wang, C.; Zhang, J. Z.; Li, Y. Hydrogen-Treated TiO₂ Nanowire Arrays for Photoelectrochemical Water Splitting. *Nano Lett.* **2011**, *11*, 3026–3033.
39. Park, J. H.; Kim, S.; Bard, A. J. Novel Carbon-Doped TiO₂ Nanotube Arrays with High Aspect Ratios for Efficient Solar Water Splitting. *Nano Lett.* **2006**, *6*, 24–28.
40. Khan, S. U. M.; Akikusa, J. Photoelectrochemical Splitting of Water at Nanocrystalline n-Fe₂O₃ Thin-Film Electrodes. *J. Phys. Chem. B* **1999**, *103*, 7184–7189.
41. Pu, Y.; Wang, G.; Chang, K.; Ling, Y.; Lin, Y.; Fitzmorris, B. C.; Liu, C.; Lu, X.; Tong, Y.; Zhang, J. Z.; Hsu, Y.; Li, Y. Au Nanostructure-Decorated TiO₂ Nanowires Exhibiting Photoactivity Across Entire UV–Visible Region for Photoelectrochemical Water Splitting. *Nano Lett.* **2013**, *13*, 3817–3823.
42. Pu, Y.; Ling, Y.; Chang, K.; Liu, C.; Zhang, J. Z.; Hsu, Y.; Li, Y. Surface Passivation of TiO₂ Nanowires Using a Facile Precursor-Treatment Approach for Photoelectrochemical Water Oxidation. *J. Phys. Chem. C* **2014**, *118*, 15086–15094.
43. Qian, F.; Wang, H.; Ling, Y.; Wang, G.; Thelen, M. P.; Li, Y. Photoenhanced Electrochemical Interaction between Shewanella and a Hematite Nanowire Photoanode. *Nano Lett.* **2014**, *14*, 3688–3693.
44. Lin, Y.; Zhou, S.; Liu, X.; Sheehan, S.; Wang, D. TiO₂/TiSi₂ Heterostructures for High-Efficiency Photoelectrochemical H₂O Splitting. *J. Am. Chem. Soc.* **2009**, *131*, 2772–2773.
45. Pradhan, D.; Mohapatra, S. K.; Tymen, S.; Misra, M.; Leung, K. T. Morphology-Controlled ZnO Nanomaterials for Enhanced Photoelectrochemical Performance. *Mater. Express* **2011**, *1*, 59–67.
46. Allam, N. K.; Poncheri, A. J.; El-Sayed, M. A. Vertically Oriented Ti–Pd Mixed Oxynitride Nanotube Arrays for Enhanced Photoelectrochemical Water Splitting. *ACS Nano* **2011**, *5*, 5056–5066.
47. Sheng, W.; Sun, B.; Shi, T.; Tan, X.; Peng, Z.; Liao, G. Quantum Dot-Sensitized Hierarchical Micro/Nanowire Architecture for Photoelectrochemical Water Splitting. *ACS Nano* **2014**, *8*, 7163–7169.
48. Hartmann, P.; Lee, D.; Smarsly, B. M.; Janek, J. Mesoporous TiO₂: Comparison of Classical Sol–Gel and Nanoparticle Based Photoelectrodes for the Water Splitting Reaction. *ACS Nano* **2010**, *4*, 3147–3154.